EJNMMI Physics

ORIGINAL RESEARCH

Open Access

Feasibility simulation study of positronium lifetime imaging with the Biograph Vision Quadra and J-PET tomographs

Szymon Parzych[1,2*], Szymon Niedźwiecki[1,2], Ermias Yitayew Beyene[1,2], Neha Chug[1,2], Maurizio Conti[3], Catalina Curceanu[4], Eryk Czerwiński[1,2], Manish Das[1,2], Kavya Valsan Eliyan[1,2], Jakub Hajduga[5], Sharareh Jalali[1,2], Krzysztof Kacprzak[1,2], Tevfik Kaplanoglu[1,2], Łukasz Kapłon[1,2], Kamila Kasperska[1,2], Aleksander Khreptak[1,2], Grzegorz Korcyl[1,2], Tomasz Kozik[1,2], Deepak Kumar[1,2], Anoop Kunimmal Venadan[1,2], Karol Kubat[1,2], Edward Lisowski[6], Filip Lisowski[6], Justyna Medrala-Sowa[1,2], Wiktor Mryka[1,2], Simbarashe Moyo[1,2], Piyush Pandey[1,2], Elena Perez del Rio[1,2], Alessio Porcelli[1], Bartłomiej Rachwał[5], Martin Rädler[1,2], Axel Rominger[7], Sushil Sharma[1,2], Kuangyu Shi[7], Magdalena Skurzok[1,2], William M. Steinberger[3], Tomasz Szumlak[5], Pooja Tanty[1,2], Keyvan Tayefi Ardebili[1,2], Satyam Tiwari[1,2], Ewa Ł. Stepień[1,2] and Paweł Moskal[1,2]

*Correspondence:
Szymon Parzych
szymon.parzych@doctoral.uj.edu.pl
[1]Faculty of Physics, Astronomy and Applied Computer Science, Jagiellonian University, ul. prof. Stanisława Łojasiewicza 11, 30-348 Kraków, Poland
[2]Center for Theranostics, Jagiellonian University, ul. Mikołaja Kopernika 40, 31-034 Kraków, Poland
[3]Siemens Medical Solutions USA, Inc., Knoxville, TN 37932, USA
[4]Laboratori Nazionali di Frascati, Via Enrico Fermi 54, 00044 Frascati, Italy
[5]AGH University of Kraków, al. Adama Mickiewicza 30, 30-059 Kraków, Poland
[6]Cracow University of Technology, Faculty of Mechanical Engineering, 31-864 Kraków, Poland
[7]Department of Nuclear Medicine, Inselspital, Bern University Hospital, University of Bern, Bern, Switzerland

Abstract

Background After its first ex-vivo and in-vivo demonstration, Positronium Lifetime Imaging (PLI) has received considerable interest as a potential new diagnostic biomarker. High sensitivity Positron Emission Tomography (PET) systems are needed for PLI since it requires simultaneous registration of annihilation photons and prompt gamma. In this simulation-based study, a feasibility of PLI with the long axial field-of-view Biograph Vision Quadra (Quadra) and the Total Body J-PET scanner was investigated.

Methods The study was performed using the GATE software. Background radiation, present within the Quadra tomograph, was added to the simulation. First, the optimal placement of the energy window for the registration of the prompt gamma was investigated. Next, the organ-wise sensitivity of Quadra was calculated for the ^{68}Ga, ^{44}Sc, ^{22}Na and ^{124}I radioisotopes. Finally, the sensitivity for the scandium isotope was compared to the sensitivities obtainable with the Total Body J-PET scanner, as well as with the modular J-PET prototype.

Results The PLI sensitivities for the Quadra with the background radiation are estimated to 9.22(3), 10.46(4), 5.91(3), and 15.39(4) cps/kBq for the ^{44}Sc, ^{68}Ga, ^{22}Na and ^{124}I radioisotopes, respectively. The highest sensitivity was obtained when the energy window for the deexcitation photon is adjacent to the energy window for the annihilation photons. In case of J-PET, the sensitivities for the ^{44}Sc were estimated to 0.062(08) and 1.714(40) cps/kBq for the modular and Total Body J-PET scanners, respectively. The determined PLI sensitivities with Quadra and the Total Body J-PET are in the order of sensitivities of metabolic PET imaging with the short axial field-of-view (∼20 cm) PET scanners based on pure positron emitter isotopes.

© The Author(s) 2026. **Open Access** This article is licensed under a Creative Commons Attribution 4.0 International License, which permits use, sharing, adaptation, distribution and reproduction in any medium or format, as long as you give appropriate credit to the original author(s) and the source, provide a link to the Creative Commons licence, and indicate if changes were made. The images or other third party material in this article are included in the article's Creative Commons licence, unless indicated otherwise in a credit line to the material. If material is not included in the article's Creative Commons licence and your intended use is not permitted by statutory regulation or exceeds the permitted use, you will need to obtain permission directly from the copyright holder. To view a copy of this licence, visit http://creativecommons.org/licenses/by/4.0/.

Conclusions The PLI sensitivity of Quadra has been computed for the ^{68}Ga, ^{44}Sc, ^{22}Na and ^{124}I radioisotopes. A sensitivity gain by a factor of 150 was estimated relative to the modular J-PET system previously used for the first in-vivo PLI. Additionally, the sensitivity for Total Body J-PET is expected to be about 30 times higher than for modular J-PET.

Keywords Positronium lifetime imaging, J-PET, Biograph Vision Quadra, Energy window technique, Sensitivity

Background

The standard procedure of Positron Emission Tomography (PET) provides a metabolic image. Traditional Standardized Uptake Value (SUV) parameter quantifies the uptake of a given marker in tissues, enabling to identify regions of pathological metabolism [1–3]. Nevertheless, current PET systems cannot yet take advantage of measuring the lifetime of the metastable positronium atom formed in the intra-molecular voids and the information that may be obtained from it [4, 5]. For this purpose, a new PET-based imaging method has been conceived [6]–Positronium Lifetime Imaging (PLI)–to provide complementary information about the nanostructure of the imaged tissues and concentrations of bio-active molecules. In particular, mean lifetime or formation probability [7–10] constitute additional and qualitatively different contrast mechanisms from SUV [11].

In [7, 11–13] it was described that positronium properties may serve as indicators which in addition to the currently used standardized uptake value, can deliver complementary diagnostic information telling about the intramolecular architecture and the concentration of oxygen. It was also shown experimentally in ex-vivo and in-vivo studies that there are differences in the positronium lifetime between myxoma tumor and adipose tissue [14], and between glioma tumor and healthy brain tissues [8]. This novel type of imaging is recently gaining interest in both laboratory and hospital research [8, 15] with its many challenges and new opportunities, e.g. analysis of positronium lifetime spectra [16, 17], PLI algorithms [18–23], double tracer imaging [24–27]. Although the requirement of three photon coincidence reduces sensitivity significantly, it may be resolved by another current trend towards the construction of long axial field-of-view PET scanners [28–34].

The first applications of both ex-vivo and in-vivo PLI were demonstrated by the Jagiellonian-PET (J-PET) collaboration [6, 8, 14]. However, the first-ever clinical PLI image of the brain presented by the J-PET collaboration suffers from the low statistics due to the utilized radionuclide (^{68}Ga) and low scanner's sensitivity [8]. Firstly, the pharmaceutical labeled with ^{68}Ga radionuclide has a low branching ratio (1.2% [35]) for β^+ decay followed by a deexcitation through the emission of a prompt gamma [36]. The administration of dedicated radiopharmaceuticals, such as ^{44}Sc radionuclide, can enhance statistics by about 76 times [34, 37, 38]. Secondly, the patient was imaged with the prototype of the J-PET tomograph–single ring only modular J-PET with 50 cm axial field-of-view (AFOV) constructed with organic scintillators [8, 39, 40]. Its sensitivity for metabolic and positronium imaging amounts to 3.4 and 0.06 cps/kBq [8]. Therefore, in this study we investigate a crystal-based system with higher interaction probability of photons.

Most of the clinically certified PET tomographs are acquiring data in the form of list-mode pairs, which limits raw data to only double coincidences. However, in order to

perform positronium imaging, a specific type of triple coincidence is required. The type of acquisition, which allows for the registration of all interactions is referred to as triggerless mode [41, 42] or singles mode [15]. Apart from the J-PET system, which works in the triggerless data acquisition mode, the PennPET Explorer in Philadelphia, USA [32, 33] as well as the recently upgraded Biograph Vision Quadra (hereinafter referred to as Quadra) tomograph from Siemens Healthineers [15] have the possibility of singles mode acquisition.

In this simulation-based study, a feasibility of positronium lifetime imaging with Quadra was investigated and compared to the J-PET scanners. We focus on PLI sensitivity, which has been identified as a major issue in the images previously presented by the J-PET collaboration and is expected to significantly improve with the crystal-based and Total-Body tomographs. Four isotopes were explored in this work: ^{68}Ga, ^{44}Sc, ^{22}Na and ^{124}I [14, 34, 37, 38, 43, 44]. The decay scheme of these radionuclides are shown in Fig. 1. The isotope of gallium was chosen due to its common use in PET imaging. The scandium radioisotope is considered due to its feasibility for positronium imaging [36]. Despite the present lack of clinical imaging applications, the ^{22}Na isotope was chosen due to its exploitation in basic research [45]. Finally, the iodine isotope was chosen for its diagnosis and treatment capabilities of thyroid cancer [46].

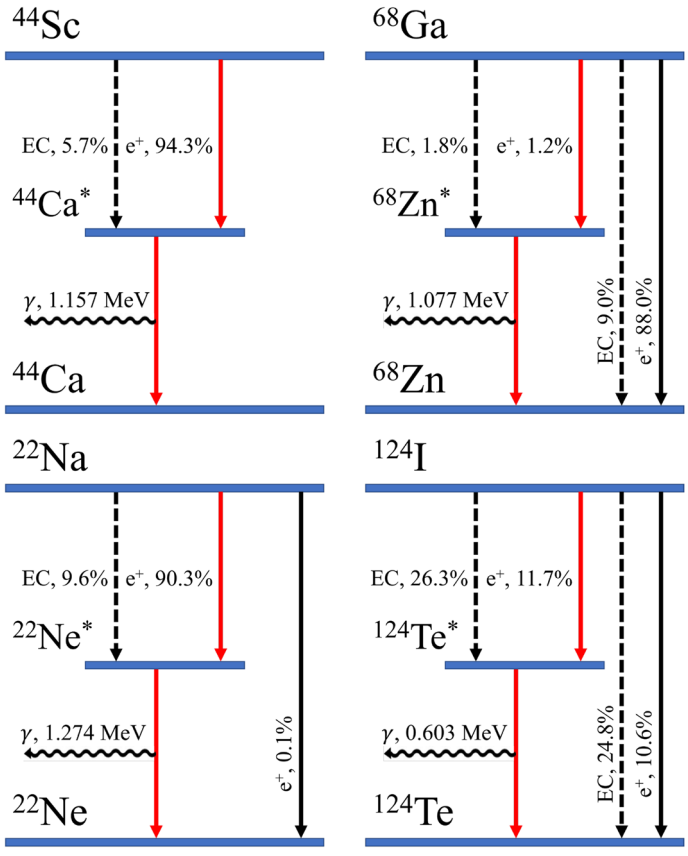


Fig. 1 Schematic of selected decay modes relevant to PET imaging for the four investigated radioisotopes: ^{44}Sc, ^{68}Ga, ^{22}Na and ^{124}I. Positron emission is denoted by e^+, whereas EC indicates the contribution from electron capture [35, 47–49]. Presented schemes show the energies of emitted deexcitation photons as well as provide percentage-based branching ratios of relevant decay channels.

Methods

Positronium imaging

The pharmaceuticals administered to the patients during PET scan are labeled with specific radioisotopes, which undergo β^+ decays. After thermalization, the emitted positron may directly annihilate with an electron from the surrounding material or create a bound, metastable atom consisting of e^+ and e^- called positronium (Ps) [45], which can be formed in one of the two states: para-positronium (p-Ps) or ortho-positronium (o-Ps), annihilating into an even or odd numbers of photons, respectively. The difference in lifetime of p-Ps and o-Ps states is especially profound in vacuum, where their respective lifetimes are 125 ps and 142 ns. Particularly, in medical purposes the ortho-positronium lifetime plays a significant role, due to its susceptibility to environmental conditions [11]. Processes such as o-Ps to p-Ps conversion or pick-off effectively shorten the Ps lifetime [45]. These alterations provide information about the intramolecular structure [9–12, 14, 45, 50, 51].

PLI has been invented in order to take advantage of positronium lifetimes alteration as a diagnostic biomarker [6, 8–10]. It employs use of a specific radioisotopes, which deexcite with the emission of a prompt gamma after the β^+ decay. A pictorial representation of PLI's principle of operation is presented in Fig. 2. Since both deexcitation and thermalization phenomena are in a similar time range (in the order of ps) and expected lifetimes are in the order of ns, registration of a prompt gamma can be treated as a timestamp of Ps formation [52, 53]. Hence, positronium lifetime may be estimated as a difference between prompt gamma emission and positronium annihilation time.

Simulation software

Simulation of radioactive β^+ decays and deexcitation of the daughter nuclei, together with tracing of their products interacting within PET tomographs, was performed with the GATE (Geant4 Application for Tomographic Emission) software (v.9.0) [54, 55]. It is an established open source software developed by the OpenGATE Collaboration for

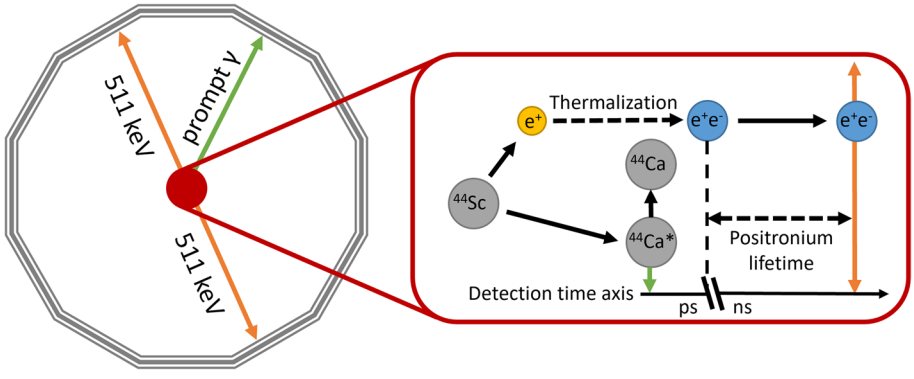


Fig. 2 Scheme of the principle of operation of positronium lifetime imaging based on the ^{44}Sc radioisotope. ^{44}Sc undergoes a β^+ decay with the emission of an electron neutrino and a positron. The radionuclide transforms into the excited state ^{44}Ca*, which then deexcites with the emission of a 1157 keV prompt gamma (marked on the main figure and the zoom with the green arrow) [34]. The emitted positron, after thermalization, may form together with an electron a bound state called positronium. In case an ortho-positronium (o-Ps) state has been created, a conversion or pick-off process results in annihilation and back-to-back emission of two 511 keV photons (marked on the main figure and the zoom with the orange arrows). Next, the annihilation photons and prompt gamma can be registered by the scintillator detectors placed in the PET scanner (gray frame). Since the expected lifetime is in order of ns, while the deexcitation time of ^{44}Ca* and the thermalization process in ps, the prompt gamma indicates the time of positronium creation [45, 52, 53]

Monte-Carlo studies in medical imaging. GATE enables the generation of three positronium decay schemes: p-Ps decaying into two photons, o-Ps decaying into three photons and a weighted mix of both p-Ps and o-Ps. However, it does not simulate interactions of atoms with medium such as conversion or pick-off process that shorten the o-Ps lifetime significantly and result in annihilations into two photons. Hence, in this study we simulated p-Ps decay into two photons and emission of prompt gamma with uncorrelated direction with respect to the propagation of annihilation photons, assuming the default lifetime in vacuum.

Studied PET scanners

This research focuses mainly on the Biograph Vision Quadra (Quadra) tomograph from the Siemens Healthineers [31], with a comparison to results achieved and possible to achieve with the modular J-PET prototype [8, 14, 39, 40, 56] and the Total Body J-PET scanner [57, 58]. Counterparts of all of the scanners were simulated with the GATE software.

Biograph Vision Quadra

The Quadra tomograph [31] utilizes $20\times3.2\times3.2$ mm^3 Lutetium Oxyorthosilicate (LSO) scintillator crystals. An array of 5×5 crystals forms a mini block, where 8 of them (2 in axial and 4 in transaxial direction) constitutes a detector block. Further, 16 blocks (2 in transaxial and 8 in axial direction) form one detector electronics assembly (DEA) (see Fig. 3). 19 DEA create one ring with 82 cm inner diameter. In total, Quadra consists of 4 rings providing a 106 cm AFOV (see Table 1). The system achieves a time-of-flight resolution of 230 ps, with a standard coincidence time window of 4.7 ns [31].

During simulation all deposited energies were smeared with a normal distribution. Following the inverse square law, its full width at half maximum (represented by resolution) was recalculated assuming a 9% resolution at an energy equal to 511 keV [31].

Modular J-PET

The modular J-PET scanner [39, 40] is built from $24\times6\times500$ mm^3 BC-404 plastic scintillator strips. Each strip is read on both ends with electronic systems. 13 axially arranged

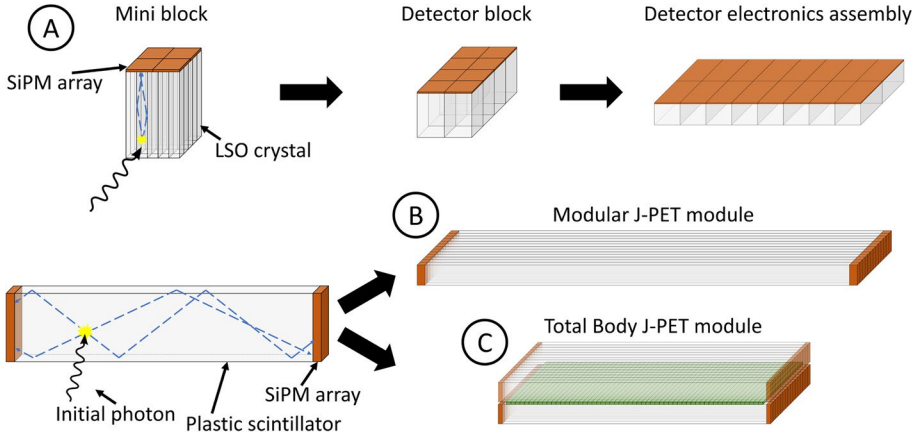


Fig. 3 **A** Scheme of the mini block, detector block and detector electronics assembly, which constitute building parts of the biograph vision quadra. **B** Modular and **C** Total body J-PET detection modules with plastic scintillators (green color marks the wavelength shifters layer)

Table 1 Geometries of the PET scanners utilized in this work

Scanner	Biograph Vision Quadra	Modular J-PET	Total body J-PET
Scintillator material	LSO	BC-404	BC-408
Scintillator dimensions [mm^3]	20×3.2×3.2	24×6×500	30×6×330
Scintillator per module*	3200	13	32 (+ WLS layer)
Modules per ring	19	24	24
Rings per scanner	4	1	7
Inner diameter [cm]	82	74	83
Axial field-of-view [cm]	106	50	243

The *Scintillator per module* row refers to the amount of scintillators present in the detector electronics assembly in Biograph Vision Quadra and module in J-PET tomographs

strips form a module (see Fig. 3), and 24 modules constitute a one layer ring scanner with an inner diameter of 74 cm. The modular J-PET has AFOV of 50 cm (see Table 1). It is equipped with the triggerless data acquisition [41, 59] enabling multi-photon tomography [14, 60] and applications of the degree of annihilation photons polarization [61, 62]. This system achieves a time-of-flight resolution of 490 ps (FWHM) [63], with a standard coincidence time window of 3 ns [56]. Its energy resolution was set during simulation to 23% at energy equal to 200 keV [42].

Total body J-PET

The simulated Total Body J-PET consists of 7 rings, each built from two layers of cylindrically arranged BC-408 plastic scintillators strips with dimensions of 30×6×330 mm^3 [64]. Every ring is constructed from 24 modules, each with 16 scintillators per layer, per ring (see Fig. 3). In total, the tomograph spans a 243 cm AFOV, with an inner diameter of 83 cm. The whole system will be set at the cross-staged gantry [65]. Moreover, an additional perpendicular layer of BC-482A wavelength shifters [66–68] is situated between the two layers of plastic strips within each module (see Table 1). The purpose of this layer is to further enhance the axial resolution of reconstructed interaction position of photons [57, 66]. The energy resolution for this system was set to 23% at an energy equal to 200 keV [42].

Energy window technique

The conventional metabolic imaging in crystal-based PET scanners focuses on registration of the 511 keV photons from e^+e^- annihilation, which interact within the scintillators via the photoelectric effect. To that end, registration of interactions is filtered via the deposited energy, which is centered around 511 keV photopeak [69]. The utilization of such an energy window (EW) allows also for immediate rejection of photons which underwent any scattering (e.g. in the patient's body), and whose involvement degrades the quality of the imaging. However, in PLI, it is necessary to register also a prompt gamma originating from radionuclide, whose initial energy for the most isotopes is higher than 511 keV [36]. Likewise, their photopeaks are situated partially or fully outside of the EW. Therefore, a second energy window needs to be introduced to register and distinguish prompt gammas. Since the EW for annihilation photons covers their highest possible energy depositions, in principle, EW for deexcitation photons may start right after the previous one and its upper limit may be left open. Hence, utilization of only the energy threshold (ET) for prompt gammas may be enough. We assume no external sources of radiation such as internal radiation (e.g. from ^{176}Lu in LSO crystals

[70]) or cosmic rays. In any case, utilization of EW and ET lead to inclusion of scattered prompt gammas, worsening the quality of gathered data. A possible approach to find the proper placement of the energy window for prompt gamma was shown in reference [56]. we adapt their nomenclature (see Fig. 4):

- energy window for annihilation photons will be denoted as the Lower Energy Window (LEW);
- energy window for prompt gamma will be called the Higher Energy Window (HEW);
- bottom energy threshold of the HEW will be named the Prompt γ Threshold.

Quadra has a well established LEW from 435 to 585 keV [31]. For isotopes with well distinguished annihilation and deexcitation photopeaks, the investigation is necessary only for the Prompt γ Threshold. However, in the case of ^{124}I isotope, which photopeaks partially overlap due to prompt gamma energy equal to 603 keV, the modification to LEW was also inspected. There, the upper limit of LEW was lowered, allowing the Prompt γ Threshold to cover more of deexcitation photopeak.

In the case of the J-PET tomographs, which are constructed from the plastic scintillators, the principle behind PET detection is switched to the Compton-based interactions [42]. Nevertheless, the same reasoning as abovementioned can be deduced by exchanging photopeak region to the Compton edge region. As shown in [56], the optimal Lower Energy Window for the ^{44}Sc radioisotope spans the 200–370 keV energy region with a closely following Prompt γ Threshold. The lower limit on LEW was previously studied [42] and doesn't depend on the utilized radioisotope (annihilation photons energy are independent of the source).

Event selection

GATE v9.0 does not support creation of triple (2 annihilation + 1 deexcitation) coincidences. Consequently, only the information on the level of Singles was saved and further analyzed in post-processing. The analysis takes as an input series of Singles sorted in time. Further, it imposes a time window to find triple coincidences. The first time window is opened with first detection. All of the next windows are opened with the

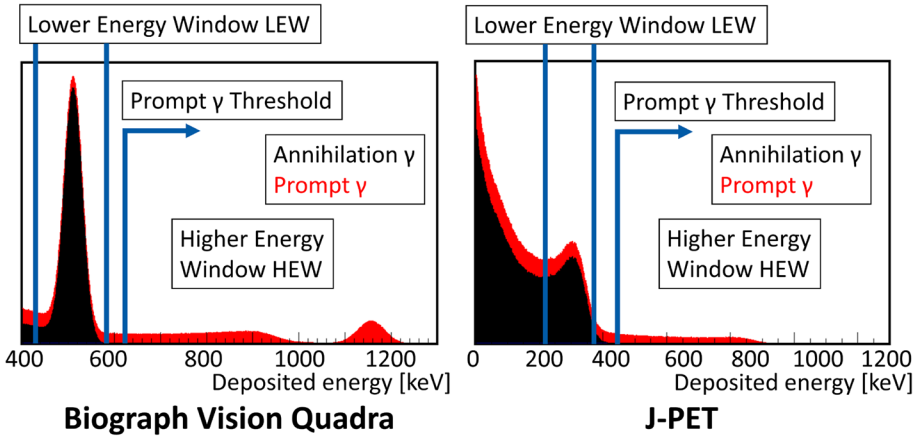


Fig. 4 Exemplary simulated energy deposition spectra for the Biograph Vision Quadra (left) and the modular J-PET (right). Red part of the spectra correspond to prompt gammas and black to annihilation photons. Moreover, exemplary positioning of Lower Energy Window for annihilation γ and Higher Energy Window for deexcitation γ (with its bottom threshold marked as Prompt γ Threshold) are denoted and marked with blue lines. The energy resolution of 9% (at 511 keV) was set for the Biograph Vision Quadra [31] and 23% (at 200 keV) for the modular J-PET [42]

subsequent detections, which did not fall into the already opened time window. If, during the time window, exactly two interactions fell into the LEW and one into the HEW, a candidate for the triple coincidence was exported.

This study focuses on the determination of system sensitivity for PLI which is independent of the positronium lifetime. Therefore, for simplicity, a default positronium lifetime in vacuum was simulated and the time windows analogical to the case of metabolic imaging were chosen: 4.7 ns and 3 ns (dictated by the geometrical acceptance) for Quadra and J-PET, respectively [31, 56]. During metabolic imaging both registered photons are emitted at the same time. However, in PLI the time window should be dictated by the lifetime of positronium in the investigated object. The mean positronium lifetime for different tissues like cardiac myxoma, adipose tissue, glioblastoma tumor, salivary glands and healthy brain tissues ranges from about 1.4–4 ns [8, 10, 14, 50, 71–78]. Therefore, in experimental positronium lifetime imaging the time window has to be extended, e.g. to 10 ns.

Data analysis

Each registered candidate for the triple coincidence may be categorized based on the discrimination of the correct photon and on annihilation-deexcitation event history. Firstly, overlapping energy spectra of annihilation and prompt gamma may cause a misidentification of annihilation photon in LEW or prompt gamma in HEW, creating improper candidate triples. The number of correct triple candidates $N_{triples}^{correct}$ (identified with the purity P_{triple}) describes a situation when 2 detections in LEW are indeed coming from annihilation and a single detection in HEW from deexcitation, following definition:

$$P_{triple} = \frac{N_{triples}^{correct}}{N_{triples}}, \tag{1}$$

where $N_{triples}$ denotes number of all registered triple coincidences. Secondly, based on annihilation-deexcitation event history, correct triple candidates may be sorted into standard coincidence types: true (with purity P_t), scattered (with purity P_s) and accidental (with purity P_a). The scattered coincidence arises when at least one of the detected photons underwent other interaction in the imaged object or detector prior to current registration. Accidental coincidence denotes a situation when at least one gamma is originating from a different annihilation-deexcitation event. The purity of true coincidences is defined as:

$$P_t = \frac{N_{triples}^{correct,\ true}}{N_{triples}^{correct}}, \tag{2}$$

where $N_{triples}^{correct,true}$ corresponds to all correct triple candidates that are not falling into scattered or accidental coincidence criterion.

For the optimization of positioning of the HEW the following figure of merit (FoM) was considered:

$$FoM = P_{triple} \times P_t \times \varepsilon_{pr}^{rel}, \tag{3}$$

where ε_{pr}^{rel} corresponds to the relative efficiency of prompt gamma registration (defined in Eq. 5).

After determining the most optimal energy windows, an organ-wise sensitivity for PLI was estimated. The organ-wise sensitivity is defined as the mean of sensitivities of slices within the ±4.5 cm region around the scanner's center. The simulation was performed using a 183 cm linear source located at the central axis of the tomograph with 1 MBq total activity. The sensitivity of the i^{th} slice ε_i was calculated based on the NEMA standards [79] as a ratio of registered true triple coincidences falling into true coincidence category originating from within the slice ($N^{correct,\ true}_{triples,\ i}$) to the activity present within it according to the following formula:

$$\varepsilon_i = \frac{R_i \times L}{d \times A}, \tag{4}$$

where L is the source length, d is the width of the slice, and A is the activity. The rate R_i of registration in counts per second is defined as $N^{correct,\ true}_{triples,\ i}$ divided by the duration of the measurement. Simulation took also into account accidental coincidences, as well as possible scatterings in the detector.

Results

Efficiency of the energy window method

In case of the metabolic imaging, the standard energy window is used to register only annihilation photons. However, if the β^+ decay is followed by a deexcitation, as in the case in PLI, an incorrect photon might be registered within the respective EW. Since the energy deposition spectra of both types of gammas may overlap, the purity of EW selection is degraded. Since Quadra has already a well established LEW for annihilation photons (435-585 keV), we only investigate the positioning and impact of HEW. Figure 5 shows the efficiency for choosing the prompt gamma in the HEW for the given energy thresholds. The relative efficiency is defined as:

$$\varepsilon^{rel}_{pr} = \frac{N_{pr}}{N^{585keV}_{pr}}, \tag{5}$$

where N_{pr} corresponds to amount of registered prompt gammas as a function of Prompt γ Threshold and N^{585keV}_{pr} denotes the reference at 585 keV. Such defined relative

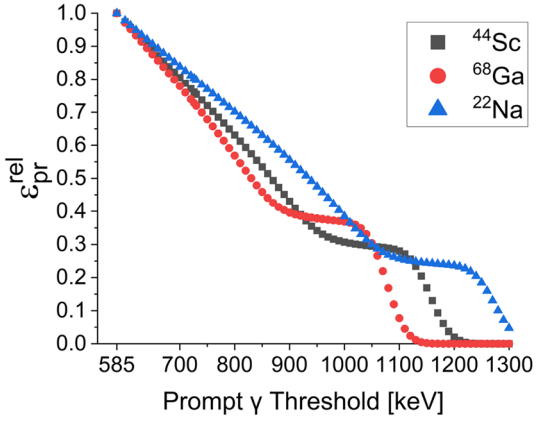


Fig. 5 Dependence of prompt gamma detection relative efficiency (ε^{rel}_{pr}) on the Prompt γ Threshold placement in the Biograph Vision Quadra for ^{44}Sc (square), ^{68}Ga (circle) and ^{22}Na (up-triangle) radioisotopes. Total of 10^8 interactions of prompt photons in the detector were simulated

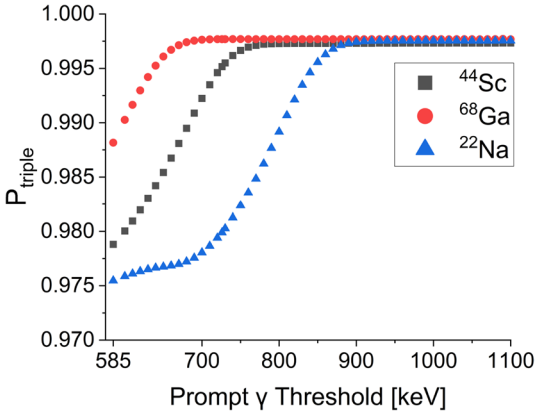


Fig. 6 Dependence of correct candidate triple selection purity (P_{triple}) on the Prompt γ Threshold for the Biograph Vision Quadra

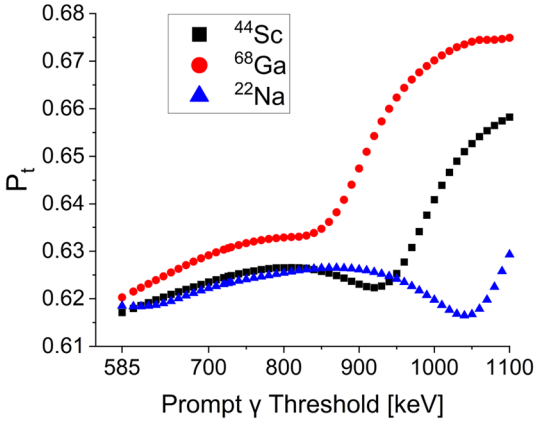


Fig. 7 Dependence of true coincidence registration probability from within correct candidate triples (P_t) on the Prompt γ Threshold for the Biograph Vision Quadra. The true coincidence requires detection of unscattered photons originating from the same annihilation-deexcitation event

efficiency is equal to 1 for the Prompt γ Threshold starting at 585 keV, right after LEW of Quadra. In all cases, the efficiency of prompt registration is falling rapidly, with a small plateau region for energies above the prompt gamma's Compton edge and below its photopeak. The ^{124}I radioisotope will be investigated separately due to modifications in its LEW.

Characteristics of triple coincidences

Figure 6 shows the purity of selecting the true candidate triples (P_{triple}). Results show high (>97%) purity of selecting such a true candidate with quick saturation. As shown in Fig. 7, the purity of registering true coincidences within the correct candidate triples slightly increases (about 1 percent) in the first half of Prompt γ Threshold range. The following drop of P_t signifies the higher impact of small-angle scattered photon registrations. The final rise of P_t corresponds to the reduction in detection of Compton interactions and scattered photons (exemplary signature shown in Fig. 8) in favor of photoelectric effect based registration of original prompt gamma. The impact of the accidental coincidences remains constant in the whole range and amounts to less than 2%, which is cause by the low simulated activity (1 MBq).

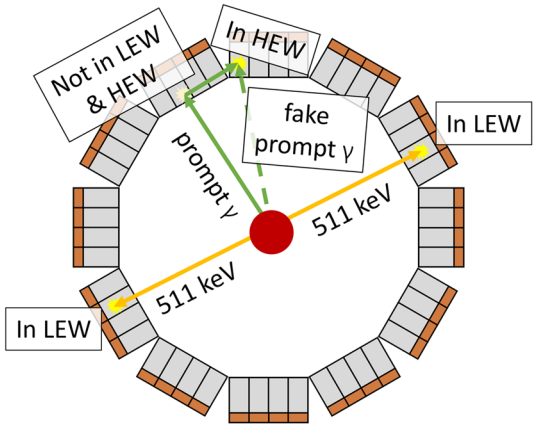


Fig. 8 Exemplary signature of correct triple coincidence falling into scattered coincidence category due to reconstruction of a fake prompt gamma

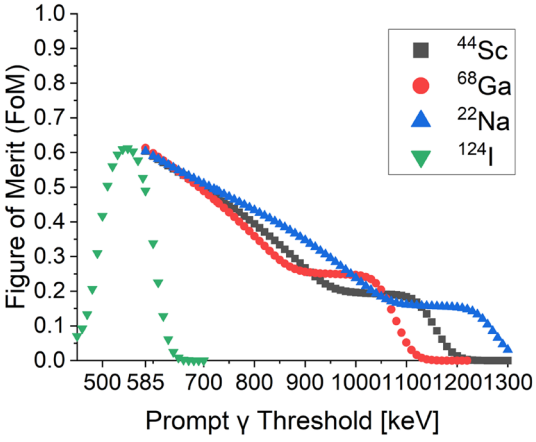


Fig. 9 Dependence of introduced figure of merit (defined in Eq. 3) on the Prompt γ Threshold for the Biograph Vision Quadra. Results for ^{44}Sc (square), ^{68}Ga (circle) and ^{22}Na (up-triangle) radioisotopes are shown. In case of ^{124}I radioisotope (down-triangle), its definition is extended to take into account the purity of prompt gamma choice (Eq. 8)

To define the optimization of the HEW the FoM from Eq. 3 was determined (Fig. 9). This variable combines the purity of choosing correct candidate triples (Fig. 6), purity of registering the true coincidence (Fig. 7), and relative efficiency for qualifying prompt gamma (Fig. 5). As all of the parameters are in range of $\langle 0, 1 \rangle$, the figure of merit takes values in the $\langle 0, 1 \rangle$ region as well. Higher values indicate better quality of data, not contaminated with scattered gammas. The resulting shape is mostly dictated by the relative efficiency (ε_{pr}^{rel}), with constant downward trend, suggesting best performance for HEW adjacent to LEW.

Case of ^{124}I radioisotope

For the iodine isotope (^{124}I), the photopeaks of annihilation and deexcitation photon overlap at each other significantly. Therefore, the upper limit of LEW was set free for the investigation of the optimal HEW, which might have started below 585 keV, hence limiting the LEW range. Consequently, the relative efficiency of prompt gamma selection has to be redefined as:

$$\varepsilon_{pr}^{rel,\ 124I} = \frac{N_{pr}}{N_{pr}^{450keV}}, \tag{6}$$

where N_{pr}^{450keV} is the number of detected prompt gammas assuming 450 keV Prompt γ Threshold. Additionally, the purity η of such threshold defined as:

$$\eta = \frac{N_{pr}}{N_{pr} + N_{ann}}, \tag{7}$$

was also checked (see Fig. 10). N_{pr} and N_{ann} correspond to amount of registered prompt and annihilation gammas respectively, with given Prompt γ Threshold. With rapidly decreasing $\varepsilon_{pr}^{rel,\ 124I}$, the inspected η well resembles the overlap between annihilation and prompt gammas' photopeaks with sigmoid-like growth saturating above 550 keV. Taking into account the purity η, the *FoM* definition is extended to:

$$FoM^{124I} = P_{triple} \times P_t \times \varepsilon_{pr}^{rel} \times \eta, \tag{8}$$

Results for P_{triple}, P_t, η and $\varepsilon_{pr}^{rel,\ 124I}$ are shown in Fig. 10, while the resulting figure of merit is presented in Fig. 9. Assuming possible variation to the LEW range, the best result can be obtained with LEW ending at 550 keV (being 45 keV lower than the Quadra threshold) and HEW starting right after.

Impact of cosmic and internal radiation on sensitivity

The LSO crystals possess intrinsic radiation originating from the lutetium ^{176}Lu isotope. ^{176}Lu decays via the β^- with a further cascade of photons with energies: 307, 202 and 88 keV [70], which can then interact within crystals leading to the creation of false coincidences. Moreover, cosmic radiation can also be registered by the tomograph. This background was added on top of the simulation output from GATE. Based on the background data gathered with the empty Biograph Vision Quadra in Inselspital in Bern, Switzerland, the time and position distribution of the background was investigated. Then, using these distributions, the background acquisition was separately simulated and transposed in post-processing onto the simulated data. Furthermore, the current acquisition in Quadra system has an upper limit on the registered energy of about 950 keV. At the same time, the energy spectrum ends at about 726 keV, where the last bin

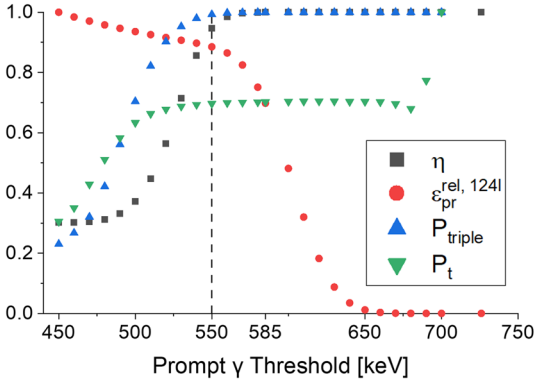


Fig. 10 Dependence of purity (η, square) and relative efficiency (ε_{pr}^{rel}, circle) of prompt gamma detection in HEW, purity of true candidate triple (P_{triple}, up-triangle) and true coincidence selection (P_t, down-triangle) on the Prompt γ Threshold for ^{124}I radioisotope examination in the Biograph Vision Quadra. The resulting figure of merit is shown in Fig. 9

Table 2 Simulated organ-wise sensitivities in cps/kBq of positronium lifetime imaging with Biograph Vision Quadra for ^{44}Sc, ^{68}Ga, ^{22}Na and ^{124}I radioisotopes The organ-wise sensitivity is defined as a mean of sensitivities of slices within the ±4.5 cm region around the scanner's center

	^{44}Sc	^{68}Ga	^{22}Na	^{124}I
Biograph Vision Quadra ideal acquisition	18.53(5)	19.23(5)	18.36(5)	15.78(4)
Biograph Vision Quadra current acquisition	9.22(3)	10.46(4)	5.91(3)	15.39(4)
Biograph Vision Quadra effective sensitivity	8.70(3)	12.55(5) $\times 10^{-2}$	5.33(3)	18.01(5) $\times 10^{-1}$

The LEW was kept at standard level of 435 keV to 585 keV, while HEW was adjacent to it (Prompt γ Threshold at 585 keV). The upper row presents results for ideal Biograph Vision Quadra data acquisition and the middle one with addition of background, upper limit at 950 keV and last bin at about 726 keV [15]. The last row takes also into account the branching ratio of the β^+ decay leading to the emission of prompt gamma equal to 94.3%, 1.2%, 90.3% and 11.7% for ^{44}Sc, ^{68}Ga, ^{22}Na and ^{124}I respectively [35, 47–49]. The presented uncertainties are statistical, and were obtained assuming Poisson distribution of counts in each slice. It is worth to mention that result obtained for ^{44}Sc is in a good agreement with the experimental value of 7.2 cps/kBq that can be determined based on the results from reference [80], although the selection criteria were not exactly the same

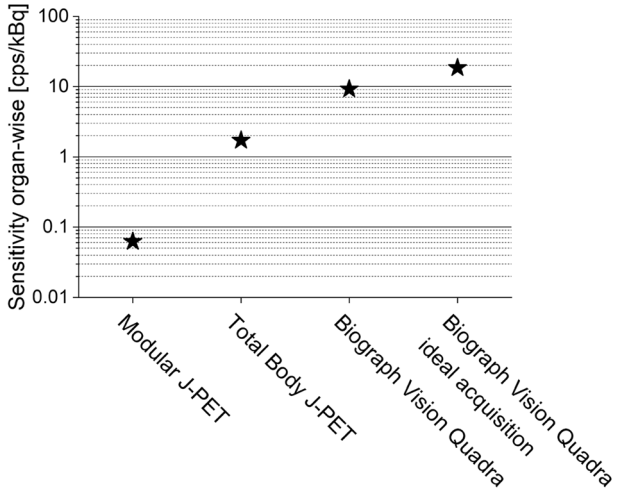


Fig. 11 The organ-wise sensitivity for positronium lifetime imaging using ^{44}Sc radioisotope estimated for the J-PET tomographs and the Biograph Vision Quadra scanner. In case of modular J-PET and Total Body J-PET the LEW was situated at 200–370 keV. For the Biograph Vision Quadra the standard LEW was utilized (435–585 keV). For all of the systems, the HEW was situated adjacent to the LEW. Calculations for the Biograph Vision Quadra were performed once assuming ideal data acquisition and once taking into account background and deposited energy measurement limitations [15]

integrates all higher depositions [15]. These limitations were also imposed on the corrected simulation. The resulting organ-wise sensitivities are presented in Table 2.

In case of J-PET tomographs: modular J-PET and Total Body J-PET, the conditions presented in [56] were simulated. Organ-wise sensitivity analysis was limited to ^{44}Sc and resulted in 0.062(08) cps/kBq for the modular J-PET and 1.714(40) cps/kBq for the Total Body J-PET. The mentioned uncertainties are statistical and derived from an assumption of Poisson distribution of counts in each slice based on the propagation of uncertainty. Comparison of the sensitivities obtained with ^{44}Sc for all studied scanners is shown in Fig. 11.

Discussion

This simulation-based research investigated the PLI sensitivity of Quadra in an effort to optimize the energy windows criterion. The study for radioisotopes ^{68}Ga, ^{44}Sc, ^{22}Na and ^{124}I, was divided into two separate cases, due to the mutual positioning of annihilation

and deexcitation photopeaks. In the case of ^{68}Ga, ^{44}Sc and ^{22}Na isotopes the prompt photopeak is well isolated. This allowed for study of only Prompt γ Threshold, while keeping the standard LEW. As shown in Fig. 6, the probability of registering a true candidate for triple coincidence is almost independent of the positioning of HEW. Despite better performance by up to 6 percents to detect true coincidences among the correct candidate triples (see Fig. 7), this benefit is insignificant compared to the deterioration of prompt gamma registration efficiency (see Fig. 5). As shown by means of the introduced FoM (see Fig. 9) the relative efficiency dictates the dependence on Prompt γ Threshold. Results indicate the best performance when positioning the HEW right after LEW at 585 keV.

Due to overlapping photopeaks in the energy spectrum of the ^{124}I radioisotope, this part of the study was conducted separately. Despite a well defined energy window for annihilation photons, its upper limit was varied in order to investigate a possible improvements in performance. In addition to all characteristics inspected previously, the purity of the prompt gamma registration in the HEW was also examined. As shown in Fig. 10, purity, probability of true candidate and true coincidence play vital roles when manipulating the LEW. Contrary, the efficiency of the deexcitation detection dominates the higher Prompt γ Threshold regions, while other factors reach a plateau. Based on the FoM from Eq. 8 (see Fig. 9), results for the HEW adjacent to the standard LEW are 20% lower then in the case of the boundary set to 550 keV.

The introduced FoM examines the impact of sensitivity for PLI. Although higher statistics has usually a positive effect on the quality of the image, further investigations, which take into account the image reconstruction are necessary to qualitatively and quantitatively address the overall impact on PLI.

A calculation of organ-wise sensitivities for Quadra (see Table 2) was performed in two different ways: assuming an ideal data acquisition and current limitations. While for the ideal situation the best results are achieved for ^{68}Ga, ^{44}Sc and ^{22}Na radioisotopes, introduction of acquisition limitations and background leads to a significant reduction (by a factor of 2-3). This is caused by the inability of photopeak registration due to hardware limitations. However, this is not an issue for ^{124}I with photopeak at 603 keV. Results show only slight alteration to the obtained sensitivity making the iodine the best performing radioisotope for the current Quadra system.

Investigations of PLI with ^{44}Sc demonstrated that the organ-wise sensitivity of Quadra is 150 times higher compared to the sensitivity of modular J-PET prototype. At the same time, the organ-wise sensitivity of PLI with the Total Body J-PET is expected to be 30 times higher [8] compared to the modular J-PET prototype.

Conclusion

The best performance suggests to place the lower edge of the HEW (Prompt γ Threshold) right after the LEW. Moreover, to optimize the sensitivity of ^{124}I, we suggest to move the upper edge of the ^{124}I LEW down to 550 keV. The performed simulations indicate that the whole-body sensitivity for PLI will be more than one order of magnitude higher for Total Body J-PET and two orders for Biograph Vision Quadra, with respect to the modular J-PET prototype used to demonstrate first in-vivo positronium lifetime images [8].

Acknowledgements
The authors would like to thank the staff of the Inselspital, Bern University Hospital who supported the background measurement utilized in this manuscript.

Author contributions
The studies were conceived by P.M. and S.P. All authors contributed to the discussions, interpretation and validation of results. Simulation of utilized systems and analysis methods were mainly developed by S.P.. P.M. and E.Ł..S. managed the whole project and secured the main financing. The early versions of results were interpreted mainly by S.P., S.N., and P.M. Reconstruction of the raw experimental data were performed by S.P., S.N. and W.M.S.. The manuscript was prepared by S.P., S.N., and P.M. and was then edited and approved by all authors.

Funding
We acknowledge support from the National Science Centre of Poland through Grants No. 2021/42/A/ST2/00423, No. 2021/43/B/ST2/02150, and No. 2022/47/I/NZ7/03112. The SciMat and qLife Priority Research Area budget under the auspices of the program Excellence Initiative–Research University at Jagiellonian University. The Research Support Module as part of the Excellence Initiative – Research University program at Jagiellonian University. PLGrid (ACK Cyfronet AGH, PLG/2024/017688 and PLG/2025/018762), and the Ministry of Science and Higher Education through Grant No. IAL/SP/596235/2023 and SPUB/SP/627733/2025, as well as the European Union through the ERC Advanced Grant POSITRONIUM No. 101199807).

Data availability
All data needed to evaluate the conclusions in the paper are present in the paper.

Declarations

Ethics approval and consent to participate
Not applicable

Consent for publication
Not applicable

Competing interests
P.M. is an inventor on a patent related to this work [patent nos.: (Poland) PL 227658, (Europe) EP 3039453, and (United States) US 9,851,456], filed (Poland) 30 August 2013, (Europe) 29 August 2014, and (United States) 29 August 2014; published (Poland) 23 January 2018, (Europe) 29 April 2020, and (United States) 26 December 2017. W.M.S, and M.C. are employees of Siemens Medical Solutions USA, Inc., and Siemens Healthineers International AG. The authors declare that they have no other conflict of interest.

Received: 14 July 2025 / Accepted: 1 July 2026
Published online: 19 July 2026

References

1. Alavi A, et al. Unparalleled and revolutionary impact of pet imaging on research and day to day practice of medicine. Bio-Algorithms and Med-Systems. 2021;17(4):203–12.
2. Schwenck J, et al. Advances in pet imaging of cancer. Nat Rev Cancer. 2023;23(7):474–90.
3. Bailey D, Townsend D, Valk P, Maisey M. Positron emission tomography basic sciences. London: Springer; 2005.
4. Vandenberghe S, Moskal P, Karp J. State of the art in total body pet. EJNMMI Physics. 2020;7:35.
5. Aide N, et al. Advances in pet/ct technology: an update. Semin Nucl Med. 2022;52(3):286–301.
6. Moskal P. Positronium imaging. In: 2019 IEEE Nuclear Science Symposium and Medical Imaging Conference (NSS/MIC). Manchester, UK: IEEE Xplore; 2020.
7. Moskal P, et al. Positronium imaging: history, current status, and future perspectives. IEEE Trans Radiat Plasma Med Sci. 2025. https://doi.org/10.1109/TRPMS.2025.3583554.
8. Moskal P, et al. Positronium image of the human brain in vivo. Sci Adv. 2024;10:eadp2840.
9. Moskal P, Stepień E. Perspectives on translation of positronium imaging into clinics. Front Phys. 2022;10:969806.
10. Moskal P, Kubicz E, Grudzień G, et al. Developing a novel positronium biomarker for cardiac myxoma imaging. EJNMMI Phys. 2023;10:22.
11. Moskal P, Jasińska B, Stepień E, Bass S. Positronium in medicine and biology. Nat Rev Phys. 2019;1:527–9.
12. Moskal P, Stepień E. Positronium as a biomarker of hypoxia. Bio-Algorithms and Med-Systems. 2021;17(4):311–9.
13. Moskal P. Quantum entanglement degree, mean positronium lifetime, and the $3\gamma/2\gamma$ annihilation-rate ratio as novel pet biomarkers for hypoxia–concept, challenges, and predictions. Bio-Algorithms and Med-Systems. 2026;22:56.
14. Moskal P, Dulski K, et al. Positronium imaging with the novel multiphoton pet scanner. Sci Adv. 2021;7:eabh4394.
15. Steinberger W, Mercolli L, et al. Positronium lifetime validation measurements using a long-axial field-of-view positron emission tomography scanner. EJNMMI Phys. 2024;11:76.
16. Dulski K. Pals avalanche - a new pal spectra analysis software. Acta Phys Pol A. 2020;137:167.
17. Shibuya K, et al. Using inverse laplace transform in positronium lifetime imaging. Phys Med Biol. 2022;67:025009.
18. Qi J, Huang B. Positronium lifetime image reconstruction for tof pet. IEEE Trans Med Imaging. 2022;41:2848.
19. Shopa R, Dulski K. Positronium imaging in j-pet with an iterative activity reconstruction and a multistage fitting algorithm. Bio-Algorithms and Med-Systems. 2023;19:54–63.
20. Chen Z, Kao C-M, Huang H-H, Lingling A. Enhanced positronium lifetime imaging through two-component reconstruction in time-of-flight positron emission tomography. Front Phys. 2024;12:2848.

21. Huang B, et al. Split: statistical positronium lifetime image reconstruction via time-thresholding. IEEE Trans Med Imaging. 2024;43(6):2148–58.
22. Huang B, Qi J. High-resolution positronium lifetime tomography by the method of moments. Phys Med Biol. 2024;69:24.
23. Huang B, et al. Fast high-resolution lifetime image reconstruction for positron lifetime tomography. Commun Phys. 2025;8:181.
24. Pratt E, Lopez-Montes A, Volpe A, et al. Simultaneous quantitative imaging of two pet radiotracers via the detection of positron–electron annihilation and prompt gamma emissions. Nat Biomed Eng. 2023;7(8):1028–39.
25. Fukuchi T, Shigeta M, et al. Image reconstruction method for dual-isotope positron emission tomography. J Instrum. 2021;16:P01035.
26. Uenomachi M, Shimazoe K, Takahashi H. A double photon coincidence detection method for medical gamma-ray imaging. Bio-Algorithms and Med-Systems. 2022;18(1):120–6.
27. Beyene E, et al. Exploration of simultaneous dual-isotope imaging with multi-photon modular j-pet scanner. Bio-Algorithms and Med-Systems. 2023;19(1):101–8.
28. Mingels C, et al. Long-axial field-of-view pet imaging in patients with lymphoma. PET Clin. 2024;19(4):495–504.
29. Badawi R, et al. First human imaging studies with the explorer total-body pet scanner. J Nucl Med. 2019;60:299–303.
30. Alberts I, et al. Long-axial field-of-view pet/ct: perspectives and review of a revolutionary development in nuclear medicine based on clinical experience in over 7000 patients. Cancer Imaging. 2023;23:28.
31. Prenosil G, Sari H, Fürstner M, Afshar-Oromieh A, Shi K, Rominger A, et al. Performance characteristics of the biograph vision quadra pet/ct system with a long axial field of view using the nema nu 2–2018 standard. J Nucl Med. 2022;63(3):476–84.
32. Dai B, et al. Performance evaluation of the pennpet explorer with expanded axial coverage. Phys Med Biol. 2023;68:095007.
33. Karp J, et al. Pennpet explorer: design and preliminary performance of a whole-body imager. J Nucl Med. 2020;61:136–43.
34. Moskal P, Stepień E. Prospects and clinical perspectives of total-body pet imaging using plastic scintillators. PET Clin. 2020;15:439–52.
35. Bé M-M, Chisté V, Dulieu C, Browne E, Chechev V, Kuzmenko N, et al. Table of radionuclides. Bureau international des poids et mesures, Pavillon de Breteuil, F-92312 Sèvres. 2013.
36. Das M, et al. Estimating the efficiency and purity for detecting annihilation and prompt photons for positronium imaging with j-pet using toy monte carlo simulation. Bio-Algorithms and Med-Systems. 2023;19(1):87–95.
37. Sitarz M, Cussonneau J-P, Matulewicz T, F H. Radionuclide candidates for β+γ coincidence pet: An overview. Appl Radiat Isot 2020;155:108898.
38. Matulewicz T. Radioactive nuclei for β+γ pet and theranostics: selected candidates. Bio-Algorithms and Med-Systems. 2021;17:235–9.
39. Tayefi Ardebili F, Moskal P. Assessing the spatial resolution of the modular j-pet scanner using the maximum-likelihood expectation-maximization (mlem) algorithm. Bio-Algorithms and Med-Systems. 2024;20:1–9.
40. Tayefi Ardebili F, Niedźwiecki S, Moskal P. Evaluation of modular j-pet sensitivity. Bio-Algorithms and Med-Systems. 2023;19(1):132–8.
41. Korcyl G, et al. Evaluation of single-chip, real-time tomographic data processing on fpga soc devices. IEEE Trans Med Imaging. 2018;37(11):2526–35.
42. Moskal P, Niedźwiecki S, et al. Test of a single module of the j-pet scanner based on plastic scintillators. Nucl Instr and Meth A. 2014;764:317–21.
43. Lång C, Habs D, Parodi K, Thirolf P. Sub-millimeter nuclear medical imaging with high sensitivity in positron emission tomography using β+γ coincidences. J Instrum. 2014;9:P01008-8.
44. Thirolf P, Lång C, Parodi K. Perspectives for highly-sensitive pet-based medical imaging using β+γ coincidences. Acta Phys Pol. 2015;127:1441–4.
45. Bass S, Mariazzi S, Moskal P, Stepień E. Colloquium: positronium physics and biomedical applications. Rev Mod Phys. 2023;95:021002.
46. Phan H, et al. The diagnostic value of ^{124}i-pet in patients with differentiated thyroid cancer. Eur J Nucl Med Mol Imaging. 2008;35:958–65.
47. Bé M-M, Chisté V, Dulieu C, Browne E, Chechev V, Kuzmenko N, et al. Table of radionuclides. Bureau international des poids et mesures, Pavillon de Breteuil, F-92312 Sèvres. 2004.
48. Bé M-M, Chisté V, Dulieu C, Browne E, Chechev V, Kuzmenko N, et al. Table of Radionuclides. Bureau international des poids et mesures, Pavillon de Breteuil, F-92312 Sèvres. 2010.
49. Bergeron D, Cessna J, Fitzgerald R, Pibida L, Zimmerman B. Standardization of i-124 by three liquid scintillation-based methods. Appl Radiat Isot 154(108849) 2019.
50. Jasińska B, Zgardzińska B, et al. Human tissues investigation using pals technique. Acta Phys Pol B. 2017;48:1737–47.
51. Bass S. Qed and fundamental symmetries in positronium decays. Acta Phys Polon B. 2019;50:1319.
52. Moskal P, Kisielewska D, Shopa R, et al. Performance assessment of the 2γ positronium imaging with the total-body pet scanners. EJNMMI Phys. 2020;7:1–16.
53. Moskal P, Kisielewska D, et al. Feasibility study of the positronium imaging with the j-pet tomograph. Phys Med Biol. 2019;64:055017.
54. Sarrut D, et al. Advanced monte carlo simulations of emission tomography imaging systems with gate. Phys Med Biol 2021;66:10TR03.
55. Sarrut D, et al. The opengate ecosystem for monte carlo simulation in medical physics. Phys Med Biol. 2022;67:184001.
56. Parzych S. Optimization of positronium imaging performance of a simulated modular j-pet scanner using gate software. Bio-Algorithms and Med-Systems. 2023;19(1):80–6.
57. Moskal P, Kowalski P, Shopa R, Raczyński L, et al. Simulating nema characteristics of the modular total-body j-pet scanner–an economic total-body pet from plastic scintillators. Phys Med Biol. 2021;66:175015.
58. Dadgar M, Parzych S, et al. Comparative studies of the sensitivities of sparse and full geometries of total-body pet scanners built from crystals and plastic scintillators. EJNMMI Phys. 2023;10:62.
59. Korcyl G, Moskal P, et al. Trigger-less and reconfigurable data acquisition system for positron emission tomography. Bio-Algorithms and Med-Systems. 2014;10:37–40.

60. Moskal P, Gajos A, M, M. Testing cpt symmetry in ortho-positronium decays with positronium annihilation tomography. Nat Comm. 2021;12:5658.
61. Moskal P, Czerwiński E, Raj J, et al. Discrete symmetries tested at 10^{-4} precision using linear polarization of photons from positronium annihilations. Nat Comm. 2024;15:78.
62. Moskal P, Kumar D, Sharma S, et al. Nonmaximal entanglement of photons from positron-electron annihilation demonstrated using a novel plastic pet scanner. Sci Adv. 2025:11:eads3046.
63. Kacprzak K, et al. Methodology for time and tot calibration of a modular j-pet scanner with prompt gamma emitters 22na and 44sc. Bio-Algorithms and Med-Systems. 2026;22:36–55.
64. Kaplon L, et al. Comparative studies of plastic scintillator strips with high technical attenuation length for the total-body j-pet scanner. Nucl Instr and Meth A. 2023;1051:168186.
65. Kaplanoglu M, Moskal P. A cross-staged gantry for total-body pet and ct imaging. Bio-Algorithms and Med-Systems. 2023;19(1):109–13.
66. Smyrski J, et al. Measurement of gamma quantum interaction point in plastic scintillator with wls strips. Nucl Instr and Meth A. 2017;851:39–42.
67. Smyrski J, et al. Application of wls strips for position determination in strip pet tomograph based on plastic scintillators. Bio-Algorithms and Med-Systems. 2014;10:59–63.
68. Georgadze A, Shivani S, Tayefi Ardebili K, Moskal P. Optimization of the wls design for positron emission mammography and total-body j-pet systems. Bio-Algorithms and Med-Systems. 2023;19(1):114–23.
69. Conti M, Eriksson L. Physics of pure and non-pure positron emitters for pet: a review and a discussion. EJNMMI Phys. 2016;3:8.
70. Teimoorisichani M, Panin V, Rothfuss H, Sari H, Rominger A, Conti M. A ct-less approach to quantitative pet imaging using the lso intrinsic radiation for long-axial fov pet scanners. Med Phys. 2022;49(1):309–23.
71. Ahn T, et al. Hierarchical nature of nanoscale porosity in bone revealed by positron annihilation lifetime spectroscopy. ACS Nano. 2021;15(3):4321–34.
72. Jean Y, et al. Applications of slow positrons to cancer research: search for selectivity of positron annihilation to skin cancer. Appl Surf Sci. 2006;252(9):3166–71.
73. Chen H, et al. Applications of positron annihilation spectroscopy to life science. Defect Diffus Forum. 2012;331:275–93.
74. Avachat A, et al. Ortho-positronium lifetime for soft-tissue classification. Sci Rep. 2024;14:21155.
75. Jasińska B, Zgardzińska B, et al. Human tissues investigation using pals technique. Acta Phys Pol A. 2017;132(5):1556–8.
76. Zgardzińska B, et al. Studies on healthy and neoplastic tissues using positron annihilation lifetime spectroscopy and focused histopathological imaging. Sci Rep. 2020;10:11890.
77. Moyo S, Moskal P, Stepień E. Feasibility study of positronium application for blood clots structural characteristics. Bio-Algorithms and Med-Systems. 2022;18(1):163–7.
78. Karimi H, et al. 3d melanoma spheroid model for the development of positronium biomarkers. Sci Rep. 2023;13:7648.
79. National Electrical Manufacturers Association: NEMA Standards Publication NU 2-2018. National Electrical Manufacturers Association, 1300 N. 17th Street, Suite 900 Rosslyn, VA 22209 2018.
80. Mercolli L, et al. First positronium lifetime imaging with scandium-44 on a long axial field-of-view pet/ct. Front Nucl Med. 2025;5:1648621.

Publisher's Note

Springer Nature remains neutral with regard to jurisdictional claims in published maps and institutional affiliations.